RSC Advances

PAPER

View Article Online
View Journal | View Issue

Cite this: *RSC Adv.*, 2018, **8**, 14488

Broadening the pore size of coal-based activated carbon *via* a washing-free chem-physical activation method for high-capacity dye adsorption†

Longxin Li, Fei Sun,* Jihui Gao,* Lijie Wang, Xinxin Pi and Guangbo Zhao

Aiming to overcome the limitations of the narrow pore size distributions of traditional activated carbon materials and to achieve wide adaptabilities towards large molecules adsorption, we herein demonstrate a new type of activated carbon with a broadened pore size distribution for high-rate and high-capacity aqueous dye molecule (Rhodamine B) adsorption. The preparation of CP-AC is achieved by a facile and one-step mineral-assisted chem-physical activation strategy from Chinese large-reserve Zhundong coal with $ZnCl_2$ and CO_2 as the activation agents. The method yields the activated carbon (CP-AC) that has a pore-size broadened hierarchical pore configuration with a high surface area and a large pore volume, favorably enabling a high-capacity Rhodamine B adsorption up to 881 mg g^{-1}, which is among the highest levels of the reported activated carbons. A sonication-assisted adsorption test further demonstrates the high-rate adsorption capability of CP-AC with Rhodamine B adsorption capacity up to 842 mg g^{-1} within 30 min (96% of the saturation capacity) while microporous activated carbon obtained by solely $ZnCl_2$ activation could just achieve a capacity of 374 mg g^{-1} within 30 min. In virtue of the low-cost resource materials and washing-free craft, this work offers a simple and green preparation strategy towards high-performance coal based activated carbons, holding great potentials for the industrial production and applications.

Received 10th March 2018
Accepted 6th April 2018

DOI: 10.1039/c8ra02127a

rsc.li/rsc-advances

1. Introduction

Porous carbon materials possess a variety of advantages such as high physicochemical compatibility, easily-tunable porosity and environmentally benign nature, which enable them to be superior candidates as adsorbents in the field of adsorption.[1] To date, various porous carbon materials including activated carbons,[2] activated carbon fibers,[3] ordered mesoporous carbons,[4] hierarchically porous carbons,[5] heteroatom doped carbons,[6,7] and porous graphenes,[8,9] have been reported and employed as adsorbents for the adsorption/storage of gaseous molecules (*e.g.* H_2, CH_4, CO_2, H_2S and volatile organic compounds), liquidus ions (*e.g.* electrolyte ions for supercapacitors) or molecules (*e.g.* organic dyes and pollutants). Among these porous carbon materials, activated carbons (ACs) derived from low-cost and naturally widespread biomass/coals, are the most often utilized materials for gaseous and liquidus adsorption due to their easily scalable production and wide applicability.[10–12]

It has been widely acknowledged that pore structure is the critical factor deciding the adsorption capacity and rate capability of ACs.[13,14] Different target adsorption species have different requirements on the pore configurations of ACs, which largely depends on the size matching between adsorbate molecules and ACs' pores. In term of small gas molecules adsorption by ACs (such as CO_2 and SO_2 with molecule diameters of 0.33 and 0.43 nm, respectively), previous studies have demonstrated that micropores,[15] especially the ultramicropores with pore size of approximately 0.7 nm,[16,17] determine the adsorption capacities of ACs. In contrast, for macromolecules with large molecule diameters (such as dye Rhodamine B with the maximum diameter of $\sim$1.5 nm),[18] ACs with broadened pore sizes are beneficial to enhance the diffusion kinetic while small-size micropores should render anabatic entrance resistance for large molecules adsorption.[19,20] Moreover, it has also been suggested that compared with the unimodal microporous ACs, the existence of hierarchical pore configurations in ACs (*e.g.* micropores and meso-/macropores combined and interconnected construction) could serve as macromolecules,[21] or hydrated ions transport,[22,23] and buffing reservoirs in liquidus systems and thus greatly improve the adsorption rate and capacity.

To date, substantial progresses have been made to prepare activated carbons based on controllable physical or chemical activation methods from a variety of biomass or coals including coconut shell,[24] orange peel,[25] bamboo fiber,[26] rice husk,[27] and sewage sludge,[28] which show incremental improvements in

---

School of Energy Science and Engineering, Harbin Institute of Technology, Harbin 150001, Heilongjiang, China. E-mail: sunf@hit.edu.cn; gaojh@hit.edu.cn

† Electronic supplementary information (ESI) available. See DOI: 10.1039/c8ra02127a

boosting the adsorption/storage capability for gaseous or liquidus pollutants. Despite these achievements in developing high surface area activated carbons, the often-utilized physical or chemical activation methods commonly lead to the resulting activated carbons with a narrow micropore distribution.[29,30] It still remains challenge to develop new strategies for preparing activated carbons with tunable pore configurations to achieve wide adaptabilities towards various adsorption requirements.

Low-grade coals possess the features of high moisture content, low calorific value and high ash content which are unfavorable factors for direct combustion,[31] nevertheless, are beneficial to preparing activated carbons due to their high reactivity potentially enabling the easy tunability of carbon structure and pore configurations. Zhundong coal is a type of recently discovered low-grade coal in the Chinese Xinjiang district with an exploitable reserve of 164 Gt,[32,33] promoting people to dig its efficient and high-value utilizations. In our recent work, an one-step ammonia activation method was utilized to prepare N-doped microporous carbons with highly controllable porosity and surface chemistry.[34]

In this work, motivated by the above-mentioned viewpoints, we demonstrate a new type of Zhundong coal derived activated carbon with a broadened pore size distribution for aqueous dye molecule (Rhodamine B) adsorption removal. The preparation is based on a facile washing-free chem-physical activation strategy which is achieved by a simple heat-treatment of the mixture of activating agent ($ZnCl_2$) and non-demineralized Zhundong raw coal with CO_2 as the reaction atmosphere. Multiple effects and benefits could be achieved in such a one-step preparation process: (i) $ZnCl_2$ plays a role in creating abundant micropores during low-temperature chemical activation stage (~500 °C); (ii) subsequent temperature-rise promotes the CO_2 physical activation (~950 °C) during which the inherent minerals in Zhundong raw coal play a crucial role of catalyst in creating mesopores; (iii) the employed high-temperature (~950 °C) enables the conversion of Zn species to element zinc vapor which releases from the resulting activated carbon, avoiding the complicated and environmentally harmful acid/water washing procedures adopted in traditional chemical activation crafts; (iv) the as-obtained activated carbon has a high surface area and particularly a hierarchical pore structure possessing both micropores and mesopores, favorably enabling a high-capacity Rhodamine B adsorption of 881 mg g^{-1}, which is among the highest levels of the reported activated carbons. Moreover, a sonication-assisted adsorption test further demonstrates the high adsorption rate of as-prepared activated carbon with Rhodamine B adsorption capacity up to 842 mg g^{-1} within 30 min (96% of the saturation capacity). In contrast, the microporous activated carbon obtained by solely $ZnCl_2$ activation could just achieve 67% of its saturation adsorption capacity within 30 min sonication-assisted adsorption.

2. Experimental

2.1 Synthesis of coal-based activated carbons

The coal-based activated carbons were prepared by a simple one-step chem-physical activation method. In a typical procedure, 3 g Zhundong raw coal without demineralization and with particle sizes less than 1 μm was mixed with $ZnCl_2$ solution with a coal to $ZnCl_2$ mass ratio of 1 : 2 to get a coal–$ZnCl_2$ mixture. Subsequently, the dried mixture was transferred into a crucible in a horizontal furnace, which was then gradually heated to 950 °C under a mixture of CO_2 and N_2 (including 160 mL min^{-1} N_2 and 40 mL min^{-1} CO_2) with a heating rate of 8 °C min^{-1}. The heat treatment procedure contained two thermostatic stages with keeping at 500 °C for 1 h and 950 °C for 1 h, respectively. After cooling down, the activated carbon based on such a chem-physical activation process was obtained and denoted as CP-AC. For comparisons, the activated carbons based on solely $ZnCl_2$ chemical activations (denoted as C-AC) or CO_2 physical activations (denoted as P-AC) were also prepared by removing CO_2 in the reaction atmosphere or discarding $ZnCl_2$ mixing step in the above-mentioned procedures. Moreover, for investigating the effect of the inherent minerals of coal on the porosity development of resulting activated carbons, demineralized Zhundong coal (experiencing a hydrochloric acid (5 M) and hydrofluoric acid (20 wt%) treatment procedures)[35] was used as precursor to obtain the activated carbon (denoted as D-CP-AC) under the same chem-physical activation process as CP-AC.

2.2 Structural characterizations

The morphology and microstructure of prepared activated carbons were analyzed using scanning electron microscopy (JSM-7500F) and transmission electron microscopy (TEM, JEM-2100), respectively. X-ray diffraction (XRD) patterns were measured on a Rigaku D/Max 2400 diffractometer using CuKa radiation (40 kV, 100 mA, $\lambda = 1.5406$ Å). Pore structure analysis was conducted using ASAP 2020 sorption analyzer by N_2 adsorption at −196 °C. The corresponding pore size distribution (PSD) was obtained from Nonlocal Density Functional Theory (NLDFT). X-ray photoelectron spectroscopy (XPS) analysis was performed on a PHI 5700 ESCA System with AlKα X-ray at 14 kV and 6 mA. Raman spectroscopy was examined on a Renishaw inVia Micro-Raman spectrometer with a 532 nm diode laser excitation. Thermogravimetric analysis (TGA) was conducted to record the weight loss of coal in CO_2 atmosphere to simulate the physical activation process.

2.3 Aqueous dye adsorption tests

To evaluate the aqueous macromolecule adsorption capabilities of the obtained activated carbons, aqueous solution of Rhodamine B (RhB) was used as target adsorption system. In a typical run, 20 mg activated carbon was mixed with 100 mL aqueous solution of Rhodamine B (RhB) with an initial concentration of 200 mg L^{-1}. The mixture was stirred in the temperature-controlled mixing platform at a stirring rate of 400 rpm over a given period of time (0–180 min) under room temperature (25 °C). After that, the supernatant was collected and the concentration of remained RhB was examined by using UV-visible spectrophotometer (at the wavelength of 554 nm). The adsorption kinetic characteristics were obtained by recording the RhB concentration changes in the supernatant with increasing adsorption time. The adsorption capacity (amount of RhB adsorbed per weight of activated carbon), q_t (mg g^{-1}) was calculated using the equation:

$$q_t = \frac{(C_0 - C_t)V}{M} \quad (1)$$

where C_0 (mg L^{-1}) is the initial RhB concentration (mg L^{-1}), C_t (mg L^{-1}) is the RhB concentration at time t (min) and M (g) is the weight of tested activated carbons. The adsorption capacities are obtained by three-time repeated tests with error analysis.

In addition, to further compare the adsorption kinetic of the prepared activated carbons, a time-shortened sonication-assisted adsorption test under a sonication power of 100 W and a frequency of 40 kHz was conducted over 0–30 min. The sonication-assisted adsorption kinetic characteristics of activated carbons were analyzed using the similar method mentioned above.

3. Results and discussion

3.1 Structural characterizations

In this section, we hope to systematically investigate the structure information of prepared activated carbons, based on which the porosity development mechanisms can be revealed. Firstly, the morphology and microstructure of Zhundong raw coal and its derived activated carbons are determined by SEM and TEM analyses, as presented in Fig. 1. Fig. 1a shows the micromorphology of Zhundong coal which is consisted of a large amount of aggregated microcrystals.[34] The amplified image in Fig. 1a inset further presents a compact stacking structure without pores in the outer surface. Fig. 1b shows the TEM image of Zhundong coal, revealing a folded laminar structure similar to multi-layer graphite.[36] Fig. 1c presents the high-resolution TEM (HRTEM) image of Zhundong coal which demonstrates an amorphous carbon nature.[37] Fig. 1d–f show the microstructure information of the CP-AC sample obtained by the chem-physical activation process from which CP-AC still exhibits an aggregated plate structure similar to Zhundong raw coal. The TEM image of CP-AC shown in Fig. 1e suggests that after the temperature-rise chem-physical activation treatment, the well-folded laminar structure of Zhundong raw coal is expanded and disorganized, largely due to the inserting and etching effects of activating agents.[38,39] The HRTEM image of CP-AC shown in Fig. 1f further demonstrates an expanded carbon structure with small pores distribution relative to the compactly amorphous carbon framework of Zhundong raw coal. For comparisons, the C-AC and P-AC samples obtained by solely chemical activation or CO_2 physical activation are also characterized as presented in Fig. 1 g–i (C-AC) and Fig. 1j–l (P-AC) which show varying degrees of structural expansion and pore development. Specifically, the chemical activated C-AC shows a lower structure expansion degree than that of physical activated P-AC. As can be seen from Fig. 1j and l, P-AC exhibits obvious pores in the outer surface (Fig. 1j inset) with pore size revealed in the HRTEM image (Fig. 1l) much larger than that of C-AC. Thus, it could be concluded that activation methods pose significant impacts on the carbon structure evolution of Zhundong coal, hence inducing different pore development patterns, which will be discussed shortly.

Nitrogen adsorption/desorption isotherms and corresponding pore size distributions are further obtained to analyze the pore structure of various Zhundong coal derived ACs, as shown in Fig. 2a–c, which demonstrate significant differences. The detailed pore parameters of prepared activated carbons are also summarized in Table 1. Fig. 2a shows the N_2 adsorption isotherms which can be generally divided into two categories. Therein, CP-AC obtained by the chem-physical activation and P-AC obtained by solely CO_2 physical activation exhibits combined characteristics of type I and IV isotherm curves, with obvious loop at a relative pressure of 0.4–0.8, indicating the co-existence of micropores, mesopores and/or macropores.[40] By contrast, C-AC-500 obtained by solely $ZnCl_2$ chemical activation under 500 °C, C-AC-950 obtained by solely $ZnCl_2$ chemical activation under 950 °C and D-CP-AC obtained by the mineral-free Zhundong coal display typical type I adsorption isotherms with significant nitrogen uptakes at a relative pressure less than 0.1 indicating the dominant microporous structure.[41,42] More specifically, during solely $ZnCl_2$ chemical activation process, $ZnCl_2$ works as dehydration reagents which selectively strip H and O away from the coal structure as H_2O or H_2, promoting the cross-linking reactions and aromatization of the carbon skeleton and commonly endowing the resulting activated carbons (C-AC-500 and C-AC-950) with narrow micropore distributions.[38,43,44] Moreover, by comparing the N_2 isotherms of C-AC-500 and C-AC-950 in Fig. 2a, the increase of chemical activation temperature is not conducive to the development of pores mainly due to the excessive etching of carbon framework.[45,46] For the solely CO_2 physically activated P-AC, it is interesting to found the existence of considerable mesopores and/or macropores, which is quite different from the traditional understanding that physical activation by H_2O or CO_2 usually leads to the formation of micropores.[39] Based on this phenomenon, we suppose the inherent minerals in precursor coals may play an important role in the development of mesopores and/or macropores. To verify this conjecture, the demineralized Zhundong raw coal was used as precursor to prepare activated carbon (denoted as D-P-AC) under the same physical activation condition as P-AC. The N_2 adsorption isotherm of D-P-AC is also obtained and illustrated in Fig. S2† which demonstrates a significant difference from the N_2 isotherm of P-AC. In particular, P-AC from mineral-rich Zhundong raw coal exhibits a hierarchical pore configuration with BET surface area and pore volume of 933 m^2 g^{-1} and 0.70 cm^3 g^{-1} while the D-P-AC from mineral-free Zhundong coal shows a dominantly microporous configuration with much lower surface area and pore volume (345 m^2 g^{-1} and 0.19 cm^3 g^{-1}, respectively), clearly demonstrating the promotion effects of inherent minerals on the development of porosity during physical activation process. In order to further explore the effects of minerals on the porosity development during the chem-physical activation process, the N_2 isotherms of CP-AC obtained from mineral-rich Zhundong raw coal and D-CP-AC derived from mineral-free Zhundong coal are compared in Fig. 2a, from which CP-AC

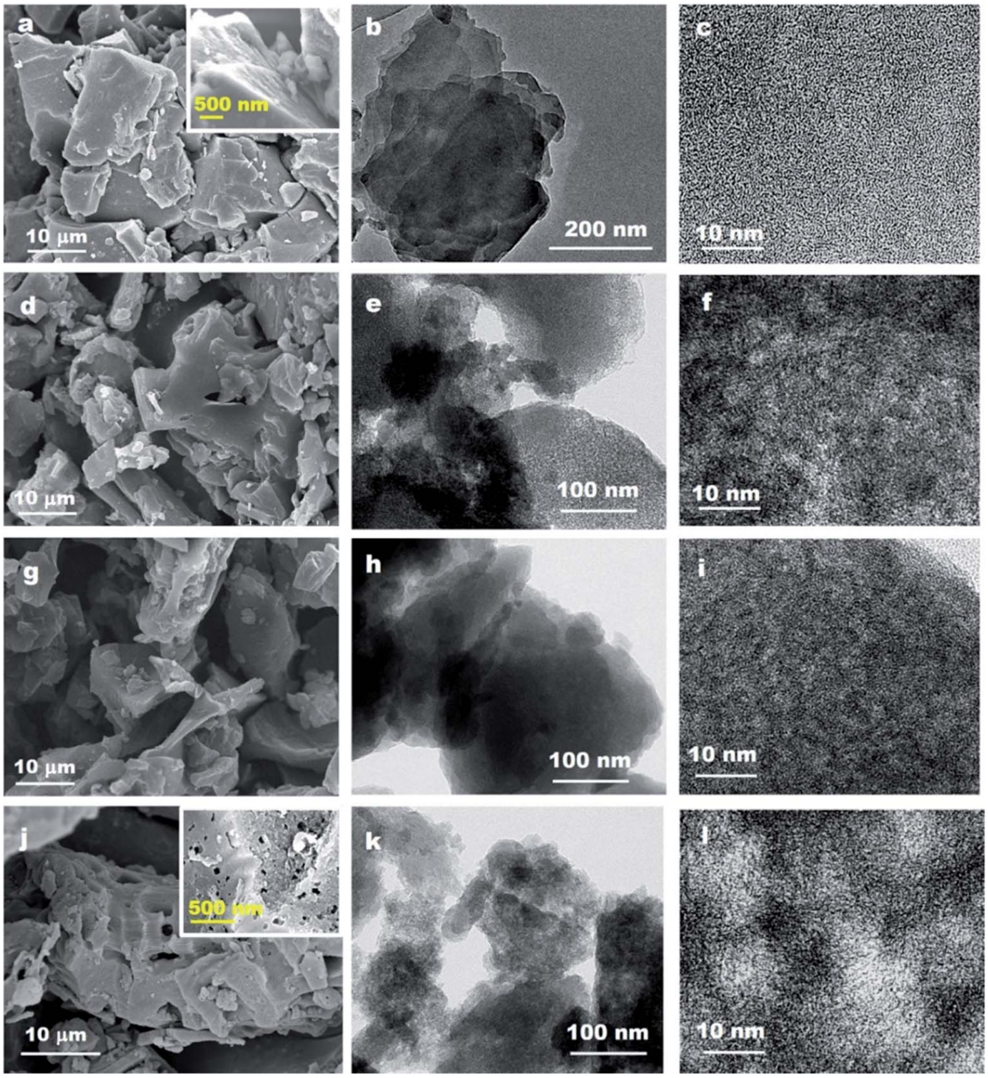

Fig. 1 SEM and TEM images of Zhundong raw coal and the derived activated carbons obtained by various activation procedures. SEM (a), TEM (b) and HRTEM (c) images of Zhundong coal; SEM (d), TEM (e) and HRTEM (f) images of CP-AC; SEM (g), TEM (h) and HRTEM (i) images of C-AC; SEM (j), TEM (k) and HRTEM (l) images of P-AC.

exhibits a hierarchically pore structure with a high N_2 adsorption amount while D-CP-AC shows a typical micropore characteristic with much lower surface area and pore volume. These results clearly demonstrate that the inherent mineral species in Zhundong coals promote the development of mesopores and/or macropores during physical activation process, endowing the resulting activated carbons (P-AC and CP-AC) with pore-size broadened hierarchical pores.

Fig. 2b further displays the corresponding DFT pore size distributions of the prepared activated carbons from which CP-AC and P-AC show obvious pore size broadening relative to other samples, demonstrating a high degree of consistency with Fig. 2a. Fig. 2c presents the pore volume distributions within various pore size ranges between the prepared activated carbons from which P-AC has the highest percentage (63%) of mesopore and macropore with CP-AC (56%) followed. In contrast, the samples obtained by solely chemical activation (C-AC-500 and C-AC-950) or demineralized coal (D-CP-AC) show obviously lower percentages of mesopores and macropores. Due to the fact that pore size is roughly in positive correlation with large pores, the average pore diameter (D_{ave}) of these activated carbons (shown in Table 1) exhibit the same variation trend with the pore volume distributions shown in Fig. 2c. It can be seen from Table 1 that among all the prepared activated carbons, CP-AC possesses the optimal pore configuration with both a micropore-mesopore combined hierarchical pore structure and the highest pore parameters (S_{BET} of 1823 $m^2\ g^{-1}$ and V_t of 0.97 $cm^3\ g^{-1}$). Such favorable pore configuration and pore parameters of CP-AC should stem from the synergistic effects of low-temperature chemical activation and high-temperature mineral-assisted physical activation during which $ZnCl_2$ etches the coal framework to form abundant micropores at low-temperature stage and CO_2 further reacts with coal framework to form mesopore and/or macropores under the role of inherent

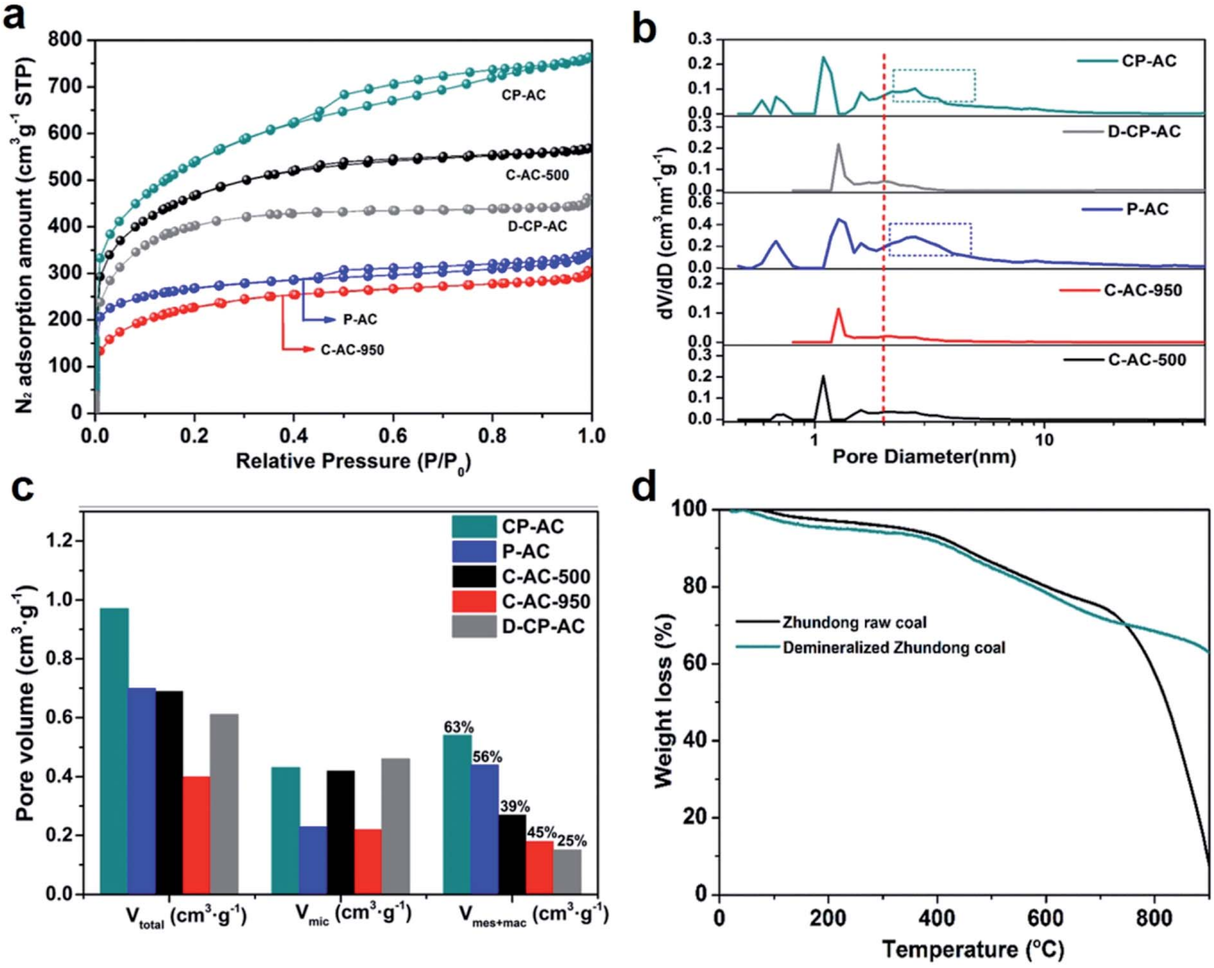

Fig. 2 (a) N_2 adsorption isotherms of prepared activated carbons; (b) DFT pore size distributions of prepared activated carbons; (c) pore volume distributions of prepared activated carbons with various pore size ranges; (d) TGA profiles of Zhundong raw coal and demineralized Zhundong coal under simulated CO_2 physical activation process.

minerals at high-temperature stage. To further dig the effect mechanism of inherent minerals on the porosity development of Zhundong coal based activated carbons in CO_2 physical activation process, thermogravimetric analyses (TGA) of Zhundong raw coal and demineralized Zhundong coal are conducted under the simulated CO_2 activation procedure, shown in Fig. 2d. It can be clearly seen that Zhundong raw coal exhibits much higher weight loss than that of demineralized Zhundong coal after the temperature reaching 700–900 °C, demonstrating the high reactivity and reaction rate of mineral-rich Zhundong raw coal with CO_2 molecules. The different TGA behaviors between Zhundong raw coal and demineralized Zhundong coal indicate that the inherent minerals in coal could greatly promote the etching reaction between CO_2 and coal structure during activation process and thus endows the resulting activated carbon with well-developed hierarchical porosities, relative to the unimodal micropore structure of demineralized Zhundong coal based activated carbon. Similar promotion

Table 1 Pore structure parameters of as-prepared activated carbons[a]

Sample	Activation conditions	S_{BET} ($m^2\ g^{-1}$)	V_{total} ($cm^3\ g^{-1}$)	V_{mic} ($cm^3\ g^{-1}$)	$V_{mec+mac}$ ($cm^3\ g^{-1}$)	D_{ave} (nm)
CP-AC	$ZnCl_2$ + CO_2 (raw coal)	1823	0.97	0.43	0.54	2.59
C-AC-500	$ZnCl_2$-500 °C (raw coal)	1529	0.69	0.42	0.27	2.30
C-AC-950	$ZnCl_2$-950 °C (raw coal)	757	0.40	0.22	0.18	2.35
P-AC	CO_2-950 °C (raw coal)	933	0.70	0.23	0.47	2.99
D-CP-AC	$ZnCl_2$ + CO_2 (demineralized coal)	1292	0.61	0.46	0.15	2.21

[a] S_{BET}: BET surface area; V_t: total pore volume obtained at P/P_0 of 0.97; V_{mic}: micropore volume obtained from the DFT accumulated pore volume with pore size less than 2 nm; $V_{mes+mac}$: mesopore and macropore volume obtained by the difference of V_t and V_{mic}; D_{ave}: average pore size determined by $4V_t/S_{BET}$.

effects of coal's inherent minerals (containing alkali and alkaline earth metals, AAEM, seeing Table S2†) have been demonstrated in the coal gasification fields that AAEMs (such as Na, K and Ca based species) could catalyze the gasification reactivity of coal/biomass with CO_2 or H_2O.[47,48]

X-ray diffraction (XRD) and Raman analyses are carried out to investigate the crystalline structures of as-obtained activated carbons by various preparation procedures. Fig. S3† gives the XRD patterns of the prepared activated carbons, all of which show two broad diffraction peaks at *ca.* 24° and 42°indicating the mainly amorphous carbon nature,[49] which is in consistent with the HRTEM results. Fig. 3a presents the Raman spectra of the activated carbons from which C-AC-500 shows the lowest I_D/I_G (0.73) among all the tested samples. Since the value of I_D/I_G represents the amorphous/disordered degree existing in the carbon matrix,[50] either increasing the chemical activation temperature (C-AC-950) or adding CO_2 into the activation procedure increases the development of amorphous or disordered structure which is in good agreement with the expanded or broken carbon framework shown in the TEM images of Fig. 1.

The chemical environments of as-obtained activated carbons are further investigated by the X-ray photoelectron spectroscopy (XPS) measurements. Fig. 3b displays the XPS overall spectra from which all the samples exhibit two peaks representing C1s and O1s signals. However, the atomic oxygen percentages between the samples show differences. C-AC-500 and CP-AC have similar oxygen contents higher than 6 at% while other samples show relatively lower oxygen percentages, indicating that high-temperature treatment or solely CO_2 physical activation should aggravate the decomposition or consumption of highly active oxygen-containing species. The chem-physical activation should be an efficient strategy to retain a relatively high oxygen content in carbon framework.

Despite the difference of oxygen contents between various samples, the O1s spectra of all the tested activated carbon can be similarly fitted to four component peaks corresponding to C═O (carboxyl) (530.6 ± 0.2 eV), C═O (ester, amides) (532.3 ± 0.3 eV), C–O–C (ester oxygen) (533.5 ± 0.2 eV) and COH, COOH (534.3 ± 0.2 eV)[51] (Fig. 3c). Fig. 3d further shows the atomic percentage of various O-containing functional groups of various

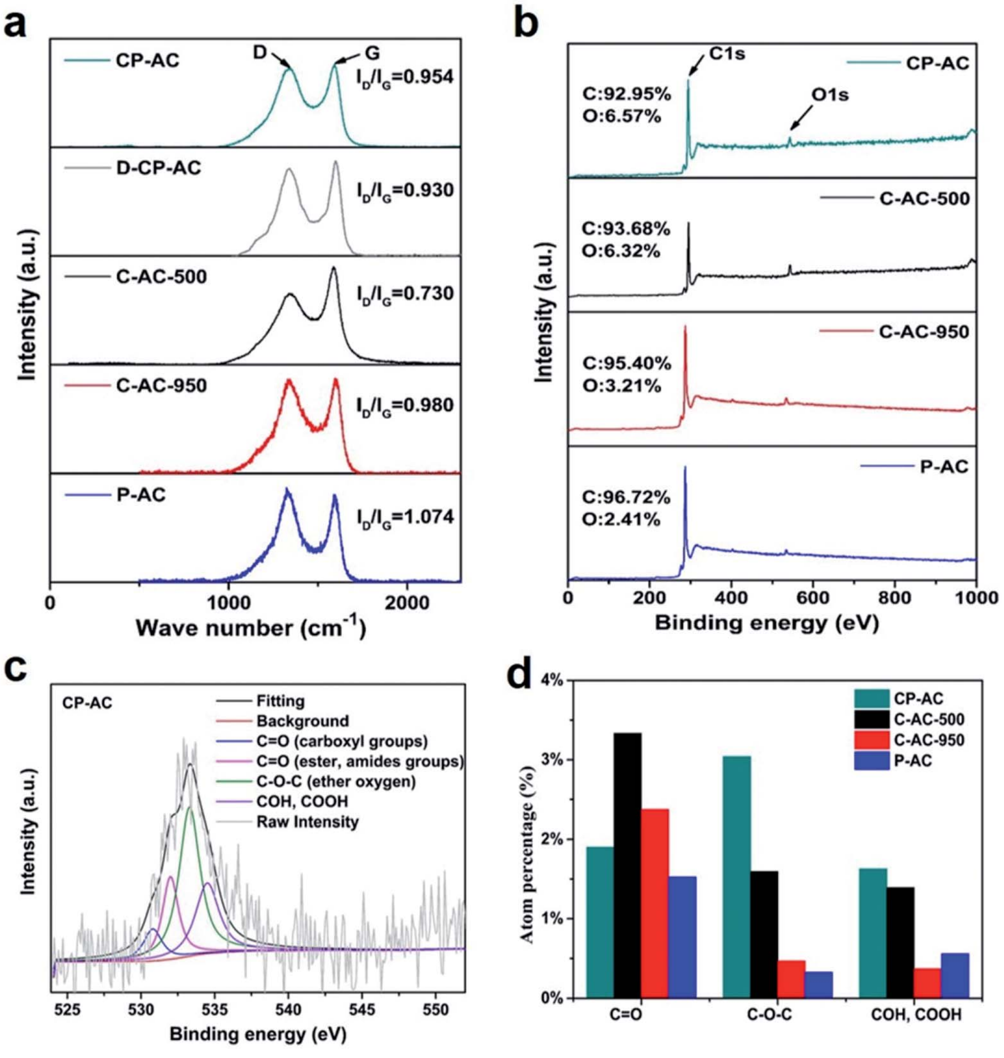

Fig. 3 (a) Raman spectra of prepared activated carbons; (b) XPS overall spectra of typical samples; (c) high-resolution O1s spectrum of CP-AC; (d) O-containing functional group distributions of typical samples.

samples from which C=O structure accounts for the majority of the total O species in each sample, indicating the similar evolution from active oxygen species to stable oxygen groups during temperature-rise activation process. Considering the similar chemical environments and BET surface area (seen Table 1) between C-AC-500 and CP-AC, these two samples give us desirable platforms to independently investigate the effects of pore configuration on the molecule adsorption, which will be discussed below.

3.2 Porosity development mechanism by mineral-catalyzed chem-physical activation

Hereto, we have demonstrated the enhancement effects of mineral-catalyzed chem-physical activation on broadening the pore size of activated carbons, leading to the CP-AC with a hierarchical pore configuration. Based on all the above-mentioned structural characterization results, the porosity development mechanism of mineral-catalyzed chem-physical activation could be summarized as illustrated in Fig. 4. The pore development schematics for activated carbons obtained by solely chemical activation or from mineral-free coal are also compared. More specifically, the mineral-assisted chem-physical activation process contains two key pore formation steps: (i) chemical activation agent $ZnCl_2$ reacts with coal framework to form abundant micropores at a low-temperature around 500 °C, during which the main reaction between $ZnCl_2$ and carbon skeleton has completed; (ii) with temperature increasing to around 950 °C, the physical activation agent CO_2 starts to react with coal framework in which the inherent minerals (especially alkali and alkaline earth metals, AAEM) play a significant role in catalyzing the etching and pore-forming reactions between CO_2 molecule and coal structure, enabling the formation of pore-size broadened mesopores.[52] These two pore formation steps are integrately achieved in one temperature-rise procedure and endow the resulting CP-AC with a favorable hierarchical pore configuration. Moreover, during the CO_2 activation stage, Zn species could convert to element zinc vapor which releases together with the off-gas,[53] thus avoiding the complicated and environmentally harmful acid/water washing procedures. By contrast, solely $ZnCl_2$ chemical activation at either high temperature or low temperature can only guide the formation of micropores (C-AC-500 and C-AC-950) while the chem-physical activation in the absence of coal's inherent minerals endure a lower reaction reactivity between coal structure and CO_2 molecules, thus also leading to the resulting D-CP-AC with unimodal micropore configuration.

3.3 RhB adsorption kinetics of Zhundong coal based activated carbons

In order to further investigate the effects of pore structure on the aqueous macromolecule adsorption capability, Rhodamine B (RhB) adsorption kinetics of the prepared activated carbons with various pore configurations (*e.g.* microporous carbons and hierarchically porous carbons) are evaluated. Fig. 5a shows the adsorption capacities as a function of time for various activated carbons within 4 h from which the adsorption kinetic process can be dissected into two stages: (i) the amount of the absorbed RhB (q_t) onto the activated carbons rapidly increases with the adsorption time from 0 to 120 min; (ii) after 120 min, the amount of the absorbed RhB (q_t) onto the activated carbons reaches a nearly constant value, indicating the adsorption equilibrium. The rapid initial adsorption rates are due to the high surface area and active sites of activated carbon and the slowly increased adsorption capabilities are due to the

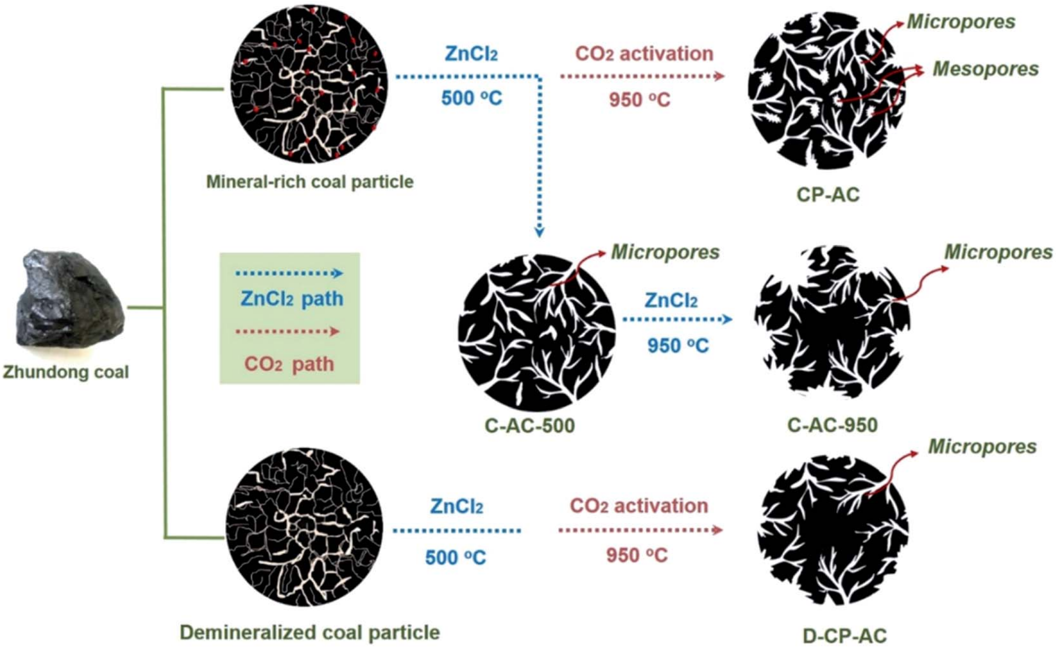

Fig. 4 A schematic illustration of the porosity development mechanism by various strategies.

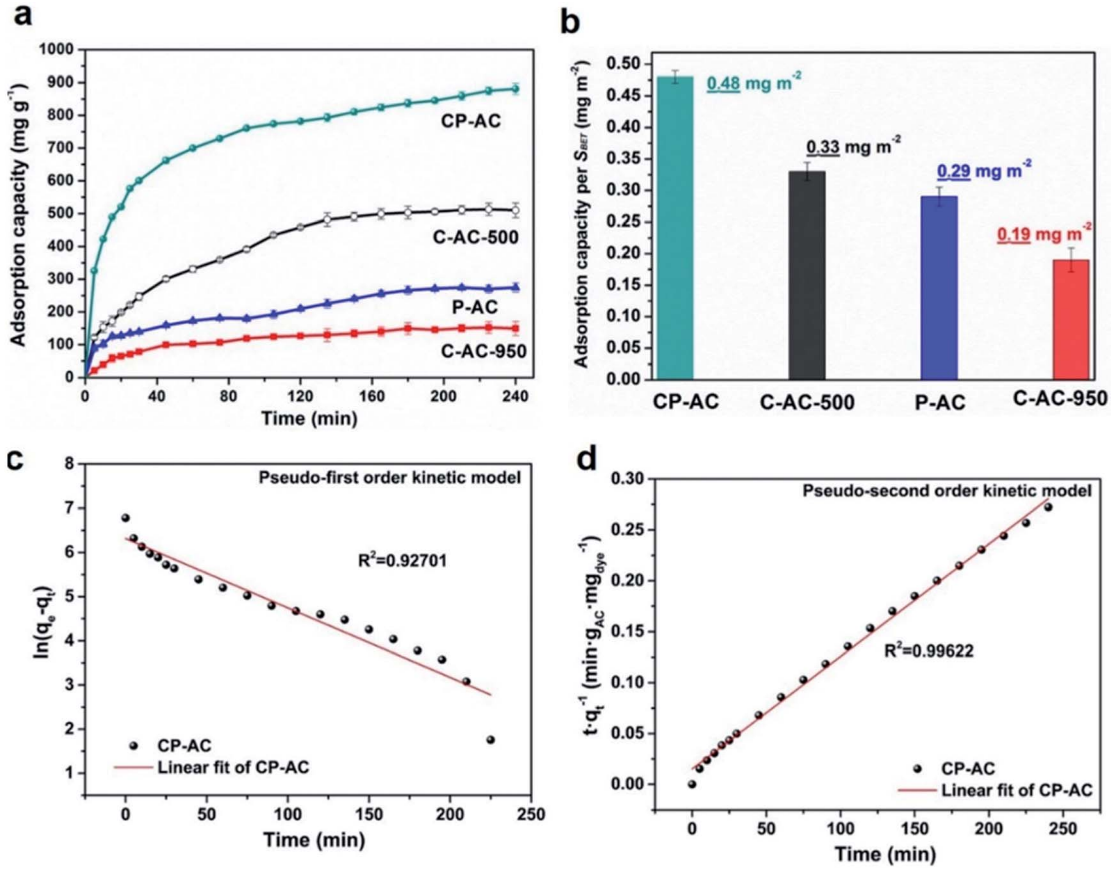

Fig. 5 RhB adsorption kinetic results of typical samples. (a) Adsorption capacities as a function of time; (b) normalized adsorption capacity to BET surface areas for typical samples; (c) pseudo-first order kinetic fitting for CP-AC; (d) pseudo-second order kinetic fitting for CP-AC.

saturation of the surface for adsorption until reaching equilibrium at 240 min. Moreover, it can be found that among the tested activated carbons, CP-AC shows much higher initial adsorption rate than that of other samples. After adsorption saturation, CP-AC also exhibits the maximum adsorption capacity up to 881.2 mg g^{-1}. Among the prepared activated carbons, CP-AC and C-AC-500 have the similar BET surface areas (seen Table 1) and chemical environments (seen Fig. 3), which give desirable platforms to independently reveal the effects of pore configuration on RhB adsorption. As can be seen from Fig. 5, C-AC-500 shows much lower adsorption rate (especially within the initial 40 min) and saturation capacity (510 mg g^{-1}), relative to those of CP-AC, which demonstrates that CP-AC with a micropore–mesopore/macropore combined hierarchical structure greatly outclasses C-AC-500 with a unimodal micropore configuration in term of RhB adsorption kinetics. For further demonstration, saturation adsorption capacities of the tested samples are normalized to their BET surface areas, which are shown in Fig. 5b. As can be observed, CP-AC shows the topmost normalized RhB adsorption capacity per surface area, clearly suggesting the improved surface area utilization. The above results indicate that the pore-size broadened hierarchical pore configuration could provide fast aqueous molecule transfer channels, adequately available surface areas and storage space, collectively endowing the CP-AC sample with the optimal RhB adsorption kinetic in terms of both adsorption rate and capacity. It is worth mentioning that such high RhB adsorption amount (881.2 mg RhB per gram activated carbon) is among the highest levels of reported porous carbons for RhB adsorption. A detailed comparison between our CP-AC sample and the reported activated carbons for RhB adsorption is summarized in Table 2.

To further reveal the kinetic adsorption model of CP-AC, pseudo-first order and pseudo-second order models investigated according to following equations:[70]

$$\text{Pseudo-first order: } \ln q_e - q_t = \ln q_e - k_1 t \tag{2}$$

$$\text{Pseudo-second order: } \frac{t}{q_t} = \frac{1}{k_2 {q_e}^2} + \frac{1}{q_e} t \tag{3}$$

where q_e and q_t (mg g^{-1}) are the amount of RhB adsorbed at equilibrium and at time t, respectively, k_1 (min^{-1}) is a rate constant of pseudo-first order adsorption, k_2 (g mg^{-1} min^{-1}) is a rate constant of pseudo-second order adsorption. Fig. 5c and d show the fitting plots for these two adsorption kinetic models. Compared with the pseudo-first order model, the R^2 value for the pseudo-second order kinetic model is close to 1.0 with the q_e value (900.9 mg g^{-1}) close to that of experimental value (881.2 mg g^{-1}), indicating that RhB adsorption on CP-AC follows the pseudo-second order kinetic model.

Table 2 Summary of RhB adsorption capabilities of literature reported activated carbons

Sample	Synthesis method	Adsorption condition (temperature, initial concentration, contact time)	Capacity/mg g^{-1}	Reference
CP-AC	**Mineral-assisted chem-physical activation**	**298 K, 200 mg L^{-1}, 4 h**	**881.2**	**This work**
HHT–ZHT–[2]P	Physico-chemical activation with $ZnCl_2$ and CO_2	Not mentioned, 1000 mg L^{-1}, not mentioned	714	54
1v4-600N	H_3PO_4 activation	293 K, 150 mg L^{-1}, 12 h	833	55
AC-SA	H_3PO_4 activation	298 K, 400 mg L^{-1}, 12 h	629.8	56
MPSC	Surfactant-templating method	303 K, 400 mg L^{-1}, 24 h	785	57
OPAC	H_3PO_4 activation	293 K, 500 mg L^{-1}, 5 h	522.11	58
PCNS–4–4	Hydrothermal method with $ZnCl_2$ activation (glucose as carbon source)	298 K, 250 mg L^{-1}, 6 h	617.8	59
C-3.5	Electrospinning with surfactant-templating method	298 K, 600 mg L^{-1}, 24 h	469	60
PK-AC	H_3PO_4 activation	293 K, 600 mg L^{-1}, 6 h	413.9	61
OAC	$ZnCl_2$ activation	318 K, 100 mg L^{-1}, 10 h	409.84	62
PA-LSAC	H_3PO_4 activation	295 K, 100 mg L^{-1}, 6 h	384.62	63
AC	H_3PO_4 activation	298 K, 100 mg L^{-1}, 1.5 h	333.33	64
Co-OMC	SBA-15 templating method	298 K, 200 mg L^{-1}, 25 min	468	65
BPH	H_3PO_4 activation	293 K, 600 mg L^{-1}, 4 h	373.8	66
LAC	KOH activation	323 K, 250 mg L^{-1}, 100 min	121.95	67
AC(H_2O)	Steam activation	298 K, 20 mg L^{-1}, 6 h	221.82	68
EAC	$ZnCl_2$ activation	298 K, 500 mg L^{-1}, 3 h	325.3	69

Since shortening adsorption time is of significance for cost-effectively industrial operation, we further employ a sonication-assisted strategy to accelerate RhB adsorption and shorten the saturation time of prepared activated carbons, which has little effect on pore structures of prepared ACs (Fig. S5, S6 and Table S3†). The adsorption time under sonication assistance is fixed at 30 min. Fig. 6a presents the adsorption capacities of CP-AC and C-AC-500 as a function of time under the 30 min sonication-assisted adsorption test, from which CP-AC achieves a high RhB adsorption capacity up to 842 mg g^{-1} within 30 min (99% of the saturation capacity) while the microporous C-AC-500 could just obtain 67% of its saturation adsorption capacity (347 mg g^{-1}), further demonstrating the adsorption kinetic advantages of hierarchically porous CP-AC over the microporous C-AC-500. Fig. 6b further illustrates the color evolutions of the supernatant with time for CP-AC and C-AC-500, which vividly demonstrate the high-rate adsorption capability of CP-AC relative to C-AC-500.

To a certain extent, no matter hierarchical pore structure or sonication-assisted adsorption, they all enhance adsorption performance by affecting diffusion resistance, which plays an important role in adsorption. Therefore, we further compare saturation adsorption test with sonication-assisted adsorption test using intraparticle diffusion model (eqn (4)) to demonstrate the difference of diffusion kinetic between the adsorption methods:

$$q_t = k_{\mathrm{id}}t^{1/2} + C \tag{4}$$

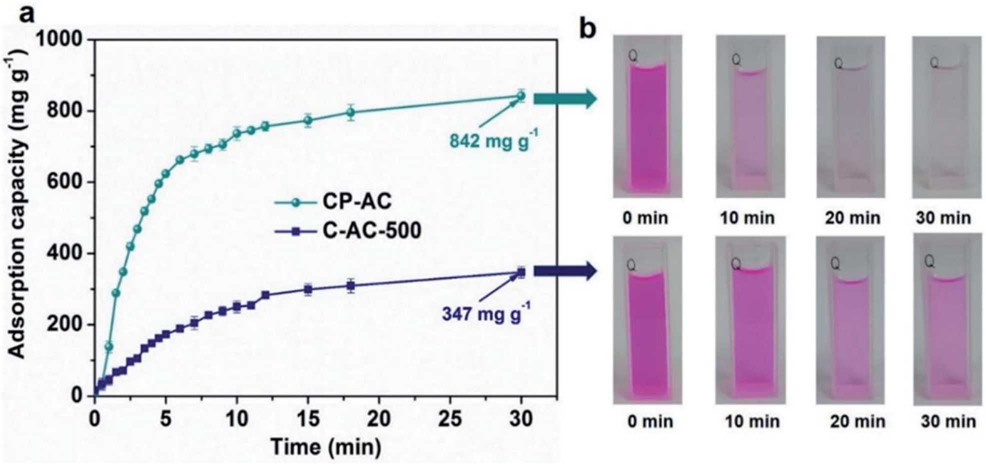

Fig. 6 (a) Adsorption capacities as a function of time under sonication-assisted adsorption test for CP-AC and C-AC-500; (b) color evolution process of supernatant with time for CP-AC and C-AC-500.

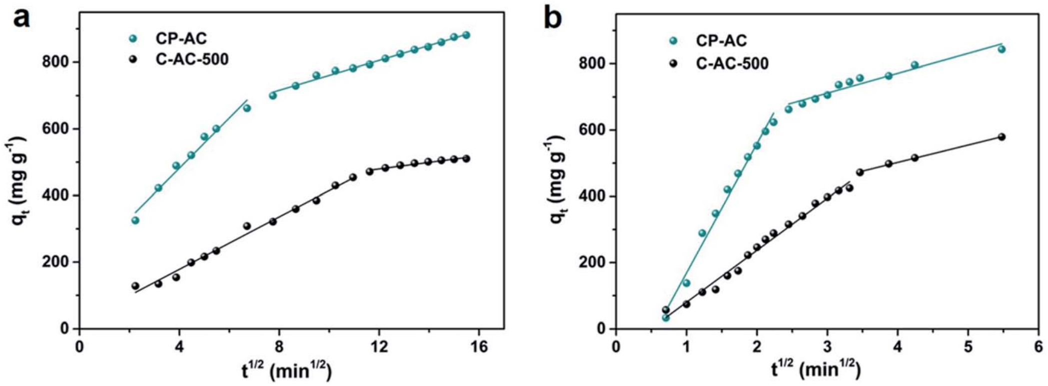

Fig. 7 RhB adsorption kinetic results of typical samples. (a) Intraparticle model fitting for saturation adsorption test; (b) intraparticle model fitting for sonication-assisted adsorption test.

where q_t and k_{id} are the amount adsorbed at time t (mg g^{-1}) and intraparticle rate constant (mg g^{-1} min$^{1/2}$). Fig. 7a and b show the fitting plots for CP-AC and C-AC-500 when using saturation adsorption test and sonication-assisted adsorption test. It can be observed that the plots are not linear over the whole time range, implying that the RhB adsorption can be divided into two steps. The adsorbate molecule rapidly enters mesopores and then penetrates more slowly into micropores,[71,72] so the intraparticle rate constants of CP-AC are higher than those of C-AC-500, indicating that hierarchical pore structures could enhance the diffusion kinetic. Table S4† summarized R^2 and intraparticle rate constant k_{id} in different adsorption methods and steps. The intraparticle rate constant k_{id} of CP-AC and C-AC-500 all increase when using sonication-assisted adsorption test, indicating that sonication could promote the diffusion of RhB molecules in CP-AC and C-AC-500. Besides, we also calculated the ratio of intraparticle rate constant k_{id} of CP-AC and C-AC-500. The ratio increased from 1.92 to 2.49 when using sonication-assisted adsorption test instead of saturation adsorption test. The increase of the ratio indicates that sonication-assisted adsorption test could better promote the diffusion kinetic when adopting the CP-AC with well-developed hierarchical pore structure. Overall, in virtue of the superior RhB adsorption kinetic combing the low-cost resource materials and simple preparation procedures, the CP-AC activated carbon holds great potentials for industrial scale-up and application for high-efficiency dye removal from water.

4. Conclusion

In summary, this work demonstrates a facile and one-step mineral-assisted chem-physical activation strategy to broaden pore size distribution of activated carbons from Chinese large-reserve Zhundong coal pursuing for high-rate and high-capacity dye molecule (Rhodamine B) adsorption. During the one-step temperature-rise process, low-temperature $ZnCl_2$ activation creates micropores and increasing temperature induces the formation of pore-size broadened mesopores under a mineral-catalyzed etching reaction between CO_2 and coal structure. As a result, the obtained activated carbon (CP-AC) features a pore-size broadened hierarchical pore configuration with a high surface area (1823 m^2 g^{-1}) and a large pore volume (0.97 cm^3 g^{-1}). Such well-developed pore structure endows the saturation adsorption capacity of Rhodamine B up to 881 mg g^{-1}, which is among the highest levels of the reported activated carbons. A sonication-assisted adsorption test further demonstrates the high-rate adsorption capability of CP-AC with Rhodamine B adsorption capacity up to 842 mg g^{-1} within 30 min (96% of the saturation capacity), while microporous activated carbon obtained by solely $ZnCl_2$ activation could just achieve a capacity of 374 mg g^{-1}.

Conflicts of interest

There are no conflicts to declare.

Acknowledgements

This research was financially supported by the National Natural Science Foundation of China (Grant No. 51376054 and 51276052).

References

1 Q. L. Ma, Y. F. Yu, M. Sindoro, A. G. Fane, R. Wang and H. Zhang, *Adv. Mater.*, 2017, **29**, 1605361.
2 C. F. Tang, Y. Shu, R. Q. Zhang, X. Li, J. F. Song, B. Li, Y. T. Zhang and D. L. Ou, *RSC Adv.*, 2017, **7**, 16092–16103.
3 W. H. Zheng, J. T. Hu, S. Rappeport, Z. Zheng, Z. X. Wang, Z. S. Han, J. Langer and J. Economy, *Microporous Mesoporous Mater.*, 2016, **234**, 146–154.
4 C. Y. Zhu and T. Akiyama, *Green Chem.*, 2016, **18**, 2106–2114.
5 L. Estevez, R. Dua, N. Bhandari, A. Ramanujapuram, P. Wang and E. P. Giannelis, *Energy Environ. Sci.*, 2013, **6**, 1785–1790.
6 G. Ma, Q. Yang, K. Sun, H. Peng, F. Ran, X. Zhao and Z. Lei, *Bioresour. Technol.*, 2015, **197**, 137–142.
7 G. Y. Xu, J. P. Han, B. Ding, P. Nie, J. Pan, H. Dou, H. S. Li and X. G. Zhang, *Green Chem.*, 2015, **17**, 1668–1674.
8 A. J. Du, Z. H. Zhu and S. C. Smith, *J. Am. Chem. Soc.*, 2010, **132**, 2876–2877.

9 J. Xiao, D. H. Mei, X. L. Li, W. Xu, D. Y. Wang, G. L. Graff, W. D. Bennett, Z. M. Nie, L. V. Saraf, I. A. Aksay, J. Liu and J. G. Zhang, *Nano Lett.*, 2011, **11**, 5071–5078.

10 N. Balahmar, A. C. Mitchell and R. Mokaya, *Adv. Energy Mater.*, 2015, **5**, 1500867.

11 B. H. Hameed and A. A. Rahman, *J. Hazard. Mater.*, 2008, **160**, 576–581.

12 H. Y. Mao, D. G. Zhou, Z. Hashisho, S. G. Wang, H. Chen, H. Y. Wang and M. J. Lashaki, *RSC Adv.*, 2015, **5**, 36051–36058.

13 W. G. Feng, S. Kwon, E. Borguet and R. Vidic, *Environ. Sci. Technol.*, 2005, **39**, 9744–9749.

14 A. S. Mestre, J. Pires, J. M. F. Nogueira, J. B. Parra, A. P. Carvalho and C. O. Ania, *Bioresour. Technol.*, 2009, **100**, 1720–1726.

15 Z. Liu, Y. Yang, Z. Du, W. Xing, S. Komarneni, Z. Zhang, X. Gao and Z. Yan, *Nanoscale Res. Lett.*, 2015, **10**, 11.

16 V. Presser, J. McDonough, S. H. Yeon and Y. Gogotsi, *Energy Environ. Sci.*, 2011, **4**, 3059–3066.

17 F. Sun, J. H. Gao, Y. W. Zhu, G. Q. Chen, S. H. Wu and Y. K. Qin, *Adsorption*, 2013, **19**, 959–966.

18 A. V. Deshpande and U. Kumar, *J. Non-Cryst. Solids*, 2002, **306**, 149–159.

19 L. Ding, V. L. Snoeyink, B. J. Marinas, Z. R. Yue and J. Economy, *Environ. Sci. Technol.*, 2008, **42**, 1227–1231.

20 F. S. Li, A. Yuasa, K. Ebie and Y. Azuma, *J. Colloid Interface Sci.*, 2003, **262**, 331–341.

21 S. M. Alatalo, E. Makila, E. Repo, M. Heinonen, J. Salonen, E. Kukk, M. Sillanpaa and M. M. Titirici, *Green Chem.*, 2016, **18**, 1137–1146.

22 J. H. Hou, C. B. Cao, F. Idrees and X. L. Ma, *ACS Nano*, 2015, **9**, 2556–2564.

23 S. X. Hu and Y. L. Hsieh, *RSC Adv.*, 2017, **7**, 30459–30468.

24 Q. Liu, M. Ke, F. Liu, P. Yu, H. Q. Hu and C. C. Li, *RSC Adv.*, 2017, **7**, 22892–22899.

25 K. Y. Foo and B. H. Hameed, *Bioresour. Technol.*, 2012, **104**, 679–686.

26 Y. Zhao, F. Fang, H. M. Xiao, Q. P. Feng, L. Y. Xiong and S. Y. Fu, *Chem. Eng. J.*, 2015, **270**, 528–534.

27 D. L. Vu, J. S. Seo, H. Y. Lee and J. W. Lee, *RSC Adv.*, 2017, **7**, 4144–4151.

28 F. S. Zhang, J. O. Nriagu and H. Itoh, *Water Res.*, 2005, **39**, 389–395.

29 A. M. Abioye and F. N. Ani, *Renewable Sustainable Energy Rev.*, 2015, **52**, 1282–1293.

30 W. M. A. W. Daud and W. S. W. Ali, *Bioresour. Technol.*, 2004, **93**, 63–69.

31 J. Y. Xu, D. X. Yu, B. Fan, X. P. Zeng, W. Z. Lv and J. Chen, *Energy Fuels*, 2014, **28**, 678–684.

32 X. H. Su, H. Jin, L. J. Guo, S. M. Guo and Z. W. Ge, *Int. J. Hydrogen Energy*, 2015, **40**, 7424–7432.

33 J. B. Zhou, X. G. Zhuang, A. Alastuey, X. Querol and J. H. Li, *Int. J. Coal Geol.*, 2010, **82**, 51–67.

34 F. Sun, J. H. Gao, Y. Q. Yang, Y. W. Zhu, L. J. Wang, X. X. Pi, X. Liu, Z. B. Qu, S. H. Wu and Y. K. Qin, *Carbon*, 2016, **109**, 747–754.

35 Y. H. Bai, Y. L. Wang, S. H. Zhu, L. J. Yan, F. Li and K. C. Xie, *Fuel*, 2014, **126**, 1–7.

36 N. G. Shang, P. Papakonstantinou, M. McMullan, M. Chu, A. Stamboulis, A. Potenza, S. S. Dhesi and H. Marchetto, *Adv. Funct. Mater.*, 2008, **18**, 3506–3514.

37 F. Sun, J. H. Gao, X. Liu, X. X. Pi, Y. Q. Yang and S. H. Wu, *Appl. Surf. Sci.*, 2016, **387**, 857–863.

38 M. A. Yahya, Z. Al-Qodah and C. W. Z. Ngah, *Renewable Sustainable Energy Rev.*, 2015, **46**, 218–235.

39 T. A. Saleh and V. K. Gupta, *Adv. Colloid Interface Sci.*, 2014, **211**, 93–101.

40 G. X. Huang, W. W. Kang, B. L. Xing, L. J. Chen and C. X. Zhang, *Fuel Process. Technol.*, 2016, **142**, 1–5.

41 M. Karthik, A. Faik, S. Doppiu, V. Roddatis and B. D'Aguanno, *Carbon*, 2015, **87**, 434–443.

42 Q. H. Liang, L. Ye, Z. H. Huang, Q. Xu, Y. Bai, F. Y. Kang and Q. H. Yang, *Nanoscale*, 2014, **6**, 13831–13837.

43 A. Ahmadpour and D. D. Do, *Carbon*, 1997, **35**, 1723–1732.

44 J. W. Kim, M. H. Sohn, D. S. Kim, S. M. Sohn and Y. S. Kwon, *J. Hazard. Mater.*, 2001, **85**, 301–315.

45 J. Hayashi, A. Kazehaya, K. Muroyama and A. P. Watkinson, *Carbon*, 2000, **38**, 1873–1878.

46 K. Mohanty, D. Das and M. N. Biswas, *Chem. Eng. J.*, 2005, **115**, 121–131.

47 R. Kopsel and H. Zabawski, *Fuel*, 1990, **69**, 275–281.

48 H. W. Wu, J. Hayashi, T. Chiba, T. Takarada and C. Z. Li, *Fuel*, 2004, **83**, 23–30.

49 D. Y. Qu, *J. Power Sources*, 2002, **109**, 403–411.

50 A. Cuesta, P. Dhamelincourt, J. Laureyns, A. Martinezalonso and J. M. D. Tascon, *Carbon*, 1994, **32**, 1523–1532.

51 M. A. Daley, C. L. Mangun, J. A. DeBarr, S. Riha, A. A. Lizzio, G. L. Donnals and J. Economy, *Carbon*, 1997, **35**, 411–417.

52 L. Wang, F. Sun, J. Gao, X. Pi, Z. Qu and G. Zhao, *Energy Fuels*, 2018, **32**, 1255–1264.

53 Z. L. Yu, G. C. Li, N. Fechler, N. Yang, Z. Y. Ma, X. Wang, M. Antonietti and S. H. Yu, *Angew. Chem., Int. Ed.*, 2016, **55**, 14623–14627.

54 A. Jain, R. Balasubramanian and M. P. Srinivasan, *Chem. Eng. J.*, 2015, **273**, 622–629.

55 Z. M. Zou, Y. Zhang, H. A. Zhang and C. H. Jiang, *RSC Adv.*, 2016, **6**, 15226–15233.

56 Z. Guo, J. Zhang and H. Liu, *RSC Adv.*, 2016, **6**, 40818–40827.

57 X. Zhuang, Y. Wan, C. Feng, Y. Shen and D. Zhao, *Chem. Mater.*, 2009, **21**, 706–716.

58 M. E. Fernandez, G. V. Nunell, P. R. Bonelli and A. L. Cukierman, *Ind. Crops Prod.*, 2014, **62**, 437–445.

59 B. Chang, D. Guan, Y. Tian, Z. Yang and X. Dong, *J. Hazard. Mater.*, 2013, **262**, 256–264.

60 Y. Dong, H. Lin, Q. Jin, L. Li, D. Wang, D. Zhou and F. Qu, *J. Mater. Chem. A*, 2013, **1**, 7391–7398.

61 L. Ding, B. Zou, W. Gao, Q. Liu, Z. Wang, Y. Guo, X. Wang and Y. Liu, *Colloids Surf., A*, 2014, **446**, 1–7.

62 O. Üner, Ü. Geçgel, H. Kolancilar and Y. Bayrak, *Chem. Eng. Commun.*, 2017, **204**, 772–783.

63 Y. Huang, X. Zheng, S. Feng, Z. Guo and S. Liang, *Colloids Surf., A*, 2016, **489**, 154–162.

64 Z. Qi, Q. Liu, Z. R. Zhu, Q. Kong, Q. F. Chen, C. S. Zhao, Y. Z. Liu, M. S. Miao and C. Wang, *Desalin. Water Treat.*, 2016, **57**, 1–13.

65 T. Lin, C. Ye, G. Yang, Y. Liu, G. Zeng, Y. Zhou, S. Li, J. Wang, S. Zhang and Y. Fang, *Appl. Surf. Sci.*, 2014, **314**, 746–753.

66 H. M. Gad and A. A. El-Sayed, *J. Hazard. Mater.*, 2009, **168**, 1070–1081.

67 D. Tolga, Ö. Yunus, E. Selim and A. B. Canan, *Fresenius Environ. Bull.*, 2011, **20**, 303–309.

68 T. Maneerung, J. Liew, Y. J. Dai, S. Kawi, C. Chong and C. H. Wang, *Bioresour. Technol.*, 2016, **200**, 350–359.

69 U. Gecgel, O. Uner, G. Goekara and Y. Bayrak, *Adsorpt. Sci. Technol.*, 2016, **34**, 512–525.

70 X. Z. Guo, P. A. Yin and H. Yang, *Microporous Mesoporous Mater.*, 2018, **259**, 123–133.

71 B. H. Hameed and F. B. M. Daud, *Chem. Eng. J.*, 2008, **139**, 48–55.

72 Z. Hu, H. Chen, F. Ji and S. Yuan, *J. Hazard. Mater.*, 2010, **173**, 292–297.